



Martian water loss to space enhanced by regional dust storms

M. S. Chaffin¹✉, D. M. Kass², S. Aoki^{3,16}, A. A. Fedorova⁴, J. Deighan¹, K. Connour¹, N. G. Heavens⁵, A. Kleinböhl², S. K. Jain¹, J.-Y. Chaufray⁶, M. Mayyasi⁷, J. T. Clarke⁷, A. I. F. Stewart¹, J. S. Evans⁸, M. H. Stevens⁹, W. E. McClintock¹, M. M. J. Crismani^{10,11}, G. M. Holsclaw¹, F. Lefevre⁶, D. Y. Lo¹², F. Montmessin⁶, N. M. Schneider¹, B. Jakosky¹, G. Villanueva¹⁰, G. Liuzzi¹⁰, F. Daerden³, I. R. Thomas³, J.-J. Lopez-Moreno¹³, M. R. Patel¹⁴, G. Bellucci¹⁵, B. Ristic³, J. T. Erwin³, A. C. Vandaele³, A. Trokhimovskiy⁴ and O. I. Korablev⁴

Mars has lost most of its initial water to space as atomic hydrogen and oxygen. Spacecraft measurements have determined that present-day hydrogen escape undergoes large variations with season that are inconsistent with long-standing explanations. The cause is incompletely understood, with likely contributions from seasonal changes in atmospheric circulation, dust activity and solar extreme ultraviolet input. Although some modelling and indirect observational evidence suggest that dust activity can explain the seasonal trend, no previous study has been able to unambiguously distinguish seasonal from dust-driven forcing. Here we present synoptic measurements of dust, temperature, ice, water and hydrogen on Mars during a regional dust event, demonstrating that individual dust events can boost planetary H loss by a factor of five to ten. This regional storm occurred in the declining phase of the known seasonal trend, establishing that dust forcing can override this trend to drive enhanced escape. Because similar regional storms occur in most Mars years, these storms may be responsible for a large fraction of Martian water loss and represent an important driver of Mars atmospheric evolution.

The desiccation and oxidation of Mars over the last 4.5 Gyr is a consequence of hydrogen loss to space¹, which was first constrained by the Mariner spacecraft². This early work established a paradigm of slow and steady H loss with little variability^{3,4}, which has been overturned with evidence for order-of-magnitude seasonal variations by Mars Express⁵, the Hubble Space Telescope^{6,7} and the Mars Atmosphere and Volatile Evolution (MAVEN) mission⁸. These later missions found that H loss from Mars peaks in southern summer, after perihelion, at rates 10–100 times higher than those in northern summer.

More recent investigations have explored the forcing of H loss by attempting to quantify the impact of seasonal drivers and relatively rare planet-encircling (also known as global) dust events on the availability of water at high altitudes. Because the data available to these studies covered a limited time period, the exact nature of the driving mechanisms was obscured and a unique attribution to seasonal versus dust effects was not made. Examination of the Mars Year 28 (2007) global dust event using a combination of dust and water ice cloud analysis and constraints from prior H loss estimates found that the effect of global events on H loss is perhaps a factor of several^{9,10}, but as the H loss was only observed to decrease simultaneously with the decline of the storm, the end of southern summer and an increase

in Mars–Sun distance, the driver of the loss could not be uniquely determined. Observations of the Mars Year 34 global event were more extensive, indicating atmospheric warming and subsequent enhancement of high-altitude water abundances and establishing that at least during global dust events water is not effectively cold-trapped by declining temperatures with increasing altitude^{11–13}. Finally, tidal¹⁴ and cloud^{15,16} observations suggest that water transport in general is strongly affected during global events, with the potential for enhanced loss. Recent observations from MAVEN's mass spectrometer indicate greater abundances of H-bearing ions during southern summer and some dust events, but do not constrain escaping hydrogen or dust abundances¹⁷.

Multiple modelling studies have predicted elevated H loss as an indirect consequence of dust activity and the resulting greater abundance of high-altitude water. One-dimensional photochemical modelling¹⁸ has shown that high-altitude water concentrations of ~100 ppm at 60 km consistent with observations^{19,20} could induce more than a tenfold increase in H loss over the course of a week. In ref. ²¹, general circulation model calculations demonstrated that interhemispheric transport in southern summer can loft water to high altitudes, and that this circulation is intensified during global dust events. Most recently, global simulations by an independent

¹Laboratory for Atmospheric and Space Physics (LASP), University of Colorado, Boulder, CO, USA. ²Jet Propulsion Laboratory, California Institute of Technology, Pasadena, CA, USA. ³Royal Belgian Institute for Space Aeronomy, Uccle, Belgium. ⁴Space Research Institute of Russian Academy of Science (IKI RAS), Moscow, Russia. ⁵Department of Atmospheric and Planetary Sciences, Hampton University, Hampton, VA, USA. ⁶Laboratoire Atmosphères, Milieux, Observations Spatiales (LATMOS), Guyancourt, France. ⁷Center for Space Physics, Boston University, Boston, MA, USA. ⁸Computational Physics Incorporated, Springfield, VA, USA. ⁹Naval Research Laboratory, Washington DC, USA. ¹⁰Goddard Space Flight Center, Greenbelt, MD, USA. ¹¹California State University San Bernardino, San Bernardino, CA, USA. ¹²Lunar and Planetary Laboratory, University of Arizona, Tucson, AZ, USA. ¹³Instituto de Astrofísica de Andalucía (IAA), Consejo Superior de Investigaciones Científicas (CSIC), Granada, Spain. ¹⁴School of Physical Sciences, The Open University, Milton Keynes, UK. ¹⁵Istituto di Astrofisica e Planetologia Spaziali (IAPS), Istituto Nazionale di Astrofisica (INAF), Rome, Italy. ¹⁶Present address: Institute of Space and Astronautical Science, Japan Aerospace Exploration Agency, Sagami-hara, Japan. ✉e-mail: michael.chaffin@colorado.edu

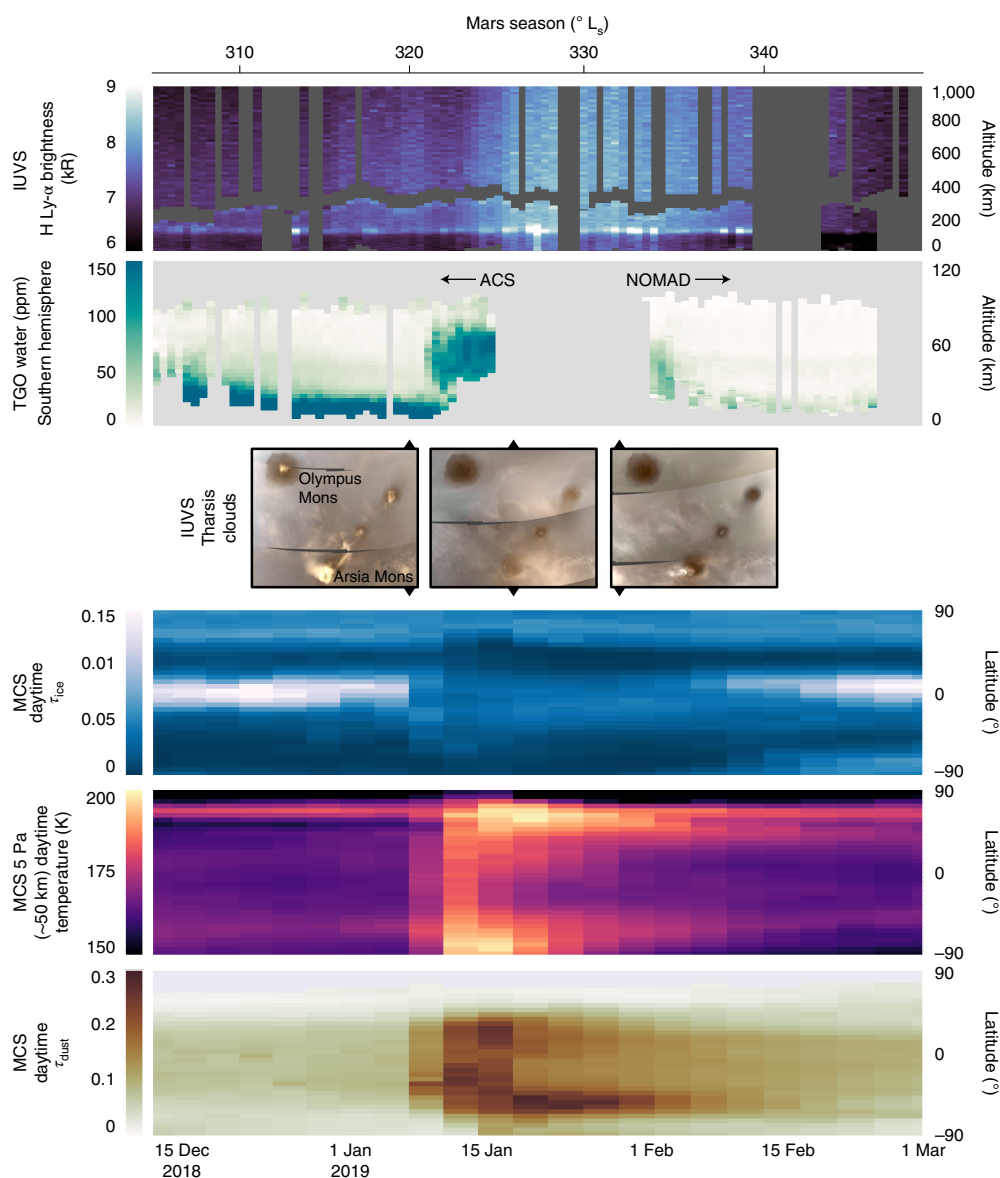


Fig. 1 | Atmospheric response to the Mars Year 34 C regional dust event. From bottom to top: dust optical depth (τ_{dust}) observed by the MCS induces a large change in mid-atmosphere temperatures and intensifies interhemispheric circulation, inhibiting ice condensation and lowering ice optical depth (τ_{ice}). IUVS observes equatorial clouds capping the Tharsis volcanoes before and after but not during the event. TGO observes the water that would have condensed into clouds at higher altitudes during the event, peaking -1 week after the beginning of the event. IUVS observes hydrogen increase in brightness by ~50% as a result of this event, consistent with an increase in H loss by a factor of several. Geometry of the IUVS and TGO observations is provided in Extended Data Figs. 1 and 2. Because this event occurred well after southern summer solstice and perihelion, we can conclude that the increase in H loss is controlled by dust dynamics rather than by seasonal changes.

group that include water photodissociation and H production demonstrate that the vertical extent of dust is a powerful control on the location of the hygropause and the ability of water to rise to altitudes where it is easily photodissociated²².

Observations of a regional dust event

In the present study, we combine data and retrieved atmospheric parameters from four instruments on three spacecraft (Fig. 1) to provide whole atmosphere measurements connecting a regional dust storm to escaping upper-atmospheric hydrogen. The Mars Climate Sounder (MCS) on the Mars Reconnaissance Orbiter (MRO)²³ is an infrared radiometer observing the 0.3–45 μm spectral range from the surface to ~90 km, retrieving atmospheric temperatures and dust and water ice opacities^{24,25}. On the Trace Gas Orbiter (TGO) mission are the Atmospheric Chemistry Suite (ACS)²⁶ and

Nadir and Occultation for Mars Discovery (NOMAD)²⁷, each of which obtains solar infrared absorption spectra at the terminator, retrieving water vapour to altitudes near 80 km (refs. ^{12,13}). Finally, MAVEN's Imaging Ultraviolet Spectrograph (IUVS)²⁸ observes neutral hydrogen in the thermosphere and corona at altitudes greater than ~100 km (ref. ²⁹). IUVS also observes the full disc of Mars, providing global images of clouds and dust.

These observations record H loss attributable to an individual lower-atmospheric dust event, which we term 'impulsive' H loss. They were made during an annually recurring C-type regional dust event (as defined in ref. ³⁰), which occurred in late southern summer of Mars Year 34 (L_s 320–336°, where the 360° L_s calendar begins with 0° at the Mars northern vernal equinox), January–February 2019. Because this storm occurred well after southern summer solstice and perihelion when the intense seasonal Hadley circulation

in the lower atmosphere and extreme ultraviolet insolation of the upper atmosphere were in decline, we can attribute the effects we observe to dust, eliminating the ambiguity in causes associated with previous observations of enhanced H loss. We present data from the Mars Year 34 C event alone because this is the only event in the MAVEN dataset for which coverage from all three spacecraft is available. Further details of the available dataset, observation geometry and retrieval techniques employed by each instrument are provided in the Methods section.

In the lower atmosphere, MRO/MCS measurements show that the regional dust event began near $L_s 320^\circ$ (Mars Year 34, 8 January 2019), close to the Acidalia–Chryse storm track ($\sim 22^\circ$ S, 32° W). The event peaked near $L_s 325^\circ$ (15 January) and declined over the next $15\text{--}20^\circ L_s$ into mid-February. Although we cannot completely rule out all potential lingering effects of the preceding global storm, the atmosphere had largely returned to a typical seasonal state before the C event onset³¹. This regional event produced a ~ 20 K temperature increase at the 5 Pa (~ 50 km) level near the equator, with a ~ 40 K increase at high southern latitudes, followed by a similar and longer-lasting increase near the north polar vortex indicative of greatly increased interhemispheric circulation. These warmer conditions observed at all latitudes inhibited ice condensation, and total column water ice opacities dropped by a factor of three during the dust event. IUVS observed this decrease in equatorial ice as the disappearance of bright clouds capping the Tharsis volcanoes, which were visible above the Rayleigh scattering of the dense lower atmosphere before and after the event but not near its peak.

In the middle atmosphere, TGO NOMAD and ACS observed little to no water at 60 km before the event. Within several sols after the dust was introduced, the mid-altitude water abundance increased by more than an order of magnitude to >100 ppm in both the ACS and NOMAD data, coinciding precisely with the disappearance of the equatorial clouds. Following the dust peak, the TGO orbit entered a period during which no occultations were possible, introducing a gap in the timeline. After occultations resumed, NOMAD retrievals indicated elevated water abundances that peaked about a scale height lower than before the gap, well into the declining phase of the event. We provide comparisons between all retrieved water abundances in Extended Data Fig. 3.

At the highest altitudes, MAVEN/IUVS observed Lyman- α sunlight scattered by H in the thermosphere and exosphere, whose brightness is a tracer of H abundance. Simultaneous with the onset of the atmospheric warming, near $L_s 322^\circ$, coronal brightnesses decreased. This indicates suppressed H densities at high altitude resulting from less effective diffusive separation of the H above the homopause, due in turn to more efficient mixing at the higher thermospheric temperatures and CO_2 densities resulting from the storm^{32,33}, similar to decreases inferred during space weather events³⁴. Immediately afterwards IUVS showed a 50% brightening at all altitudes, indicating an increase in H abundance resulting from chemical processing of mid-altitude water in the mesosphere and thermosphere. The fact that we are able to observe dimming from the dynamical process before the chemically driven H increase indicates that thermal effects of the dust event precede chemical effects in influencing the thermosphere. The peak H response occurred nearly one week after water appeared at 60 km, roughly coincident with predictions of simple photochemical models¹⁸. Based on previous modelling of the optically thick Mars corona^{5,7,35,36}, this 50% brightening corresponds to a factor of 5–10 increase in the thermospheric H abundance and a corresponding increase in the H loss rate. Greatly enhanced proton aurora near 150 km in the IUVS observations independently attest to higher H loss, as the brighter aurora are best explained by a denser upstream corona more efficiently converting solar wind protons into energetic neutrals that collide with the thermosphere and emit Lyman- α light^{37,38}.

Consequences for Mars evolution

The net result of the Mars Year 34 C-type event was a fivefold to tenfold increase in H loss across $\sim 20^\circ L_s$ (~ 40 sols), reversing the declining seasonal trend (Fig. 2). The H loss impact of individual events such as this one is comparable to the known annual trend, which peaks in southern summer with loss rates at least 20 times higher than those in southern winter⁸. Although it is likely that the magnitude of the H loss response to dust events is controlled to some degree by their strength, this response is almost certainly nonlinear on the basis of the available evidence. During the Mars Year 28 planet-encircling event, ref. ⁹ used data from earlier H loss studies^{5,6} that demonstrated a factor of 10–100 decline in the wake of the Mars Year 28 storm, but could not constrain the onset of the storm due to a lack of coronal measurements. The Heavens study⁹ also inferred hygropause altitudes and water vapour concentrations at high altitude that are comparable to our measurements by using indirect techniques that produce overestimates relative to TGO measurements (Methods), indicating that some global events are no more effective at lofting water than regional storms. By contrast, during the Mars Year 34 planet-encircling event, middle-atmosphere water abundances retrieved by ACS and NOMAD were 50–100% higher than the abundances we report for the regional event^{12,13}, suggesting potentially higher H loss rates during that global event, for which we do not have H loss measurements. Restricting our attention to C-type events only, the Mars Year 34 event was among the strongest 25% of these events well measured from orbit³⁹, suggesting that it might have a larger impact on loss than a typical C event. During Mars Year 33, a year with typical dust activity, indirect observations from ref. ⁸ suggest a 50% increase in coronal H inventory coincident with the timing of the C-type dust event, much smaller than the fivefold to tenfold increase we report here. However, the indirect technique employed in this previous work does not account for variations in atmospheric temperature known to accompany dust events³².

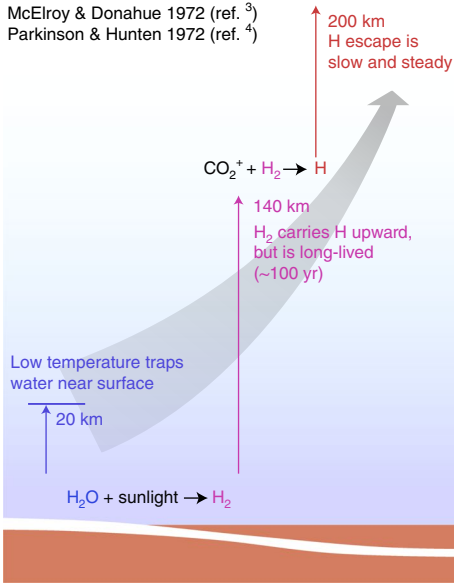
The available data suggest that regional dust events on Mars have a significant and perhaps dominant impact on H escape. Comparison of the Mars Year 28 global event and the Mars Year 34 C-type event suggests that above a certain strength, dust events have a similar impact on H loss, with each event potentially producing a 50% increase in annual H loss over a hypothetical year with no coronal response. According to ref. ³⁰, C-type and A-type dust activities capable of producing a significant northern temperature response due to enhanced interhemispheric circulation occur on average 1–2 times per Mars year, during which high-altitude water transport and H loss are likely to be enhanced across $15\text{--}40^\circ L_s$ for A-type events and $3\text{--}15^\circ L_s$ for C-type events. B-type events are less likely to drive enhanced loss because their impact is confined to the southern hemisphere, though this has yet to be definitively established. Although planet-encircling events typically last longer than regional events ($45\text{--}60^\circ L_s$), they occur only about every three Mars years³⁹, so their impact on H loss is likely to be comparable to or smaller than that of A-type and C-type regional events, if all such regional events have a similar effect on H loss.

Future work should focus on establishing the mechanism for water lofting during dust events using both observation and modelling. Although dust heating will certainly increase the altitude of the hygropause, it is not yet clear how water is actually transported to middle-atmospheric and upper-atmospheric altitudes. Several proposals exist, including orographic lifting and dusty deep convection⁴⁰. Based on the strong H loss response we observe to middle-atmospheric water, water transport to the middle atmosphere is likely to be the limiting step in the H escape chain, rather than the dissociation of water into H and O, diffusion of H through the thermosphere, or the energization of escaping H atoms. These other processes should all respond roughly linearly to an influx of

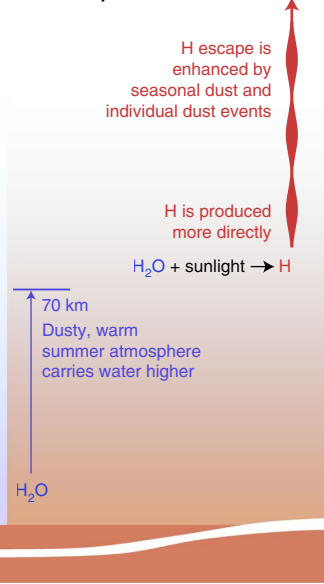
The Mars hydrogen cycle

Traditional scheme

McElroy & Donahue 1972 (ref. ³)
Parkinson & Hunten 1972 (ref. ⁴)



New concept



Seasonal versus impulsive loss

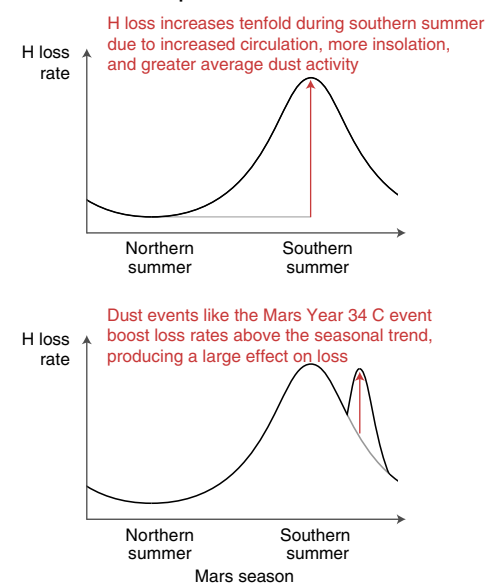


Fig. 2 | Paradigm for dust-driven and seasonal versus impulsive escape at Mars. In the traditional scheme (left), H loss is regulated by the slow and steady diffusion of molecular hydrogen to the upper atmosphere, with minimal changes in the loss rate with season or lower-atmospheric conditions. In the emerging paradigm for H loss (centre), seasonal or impulsive changes in dust can loft water to high altitude where it can directly boost escape. Top right: H loss from Mars peaks in southern summer because of seasonal changes associated with the solstice and perihelion, increased interhemispheric circulation, greater average dust activity and greater insolation. Bottom right: for this work, we are able to distinguish impulsive loss due to the C-type dust event from seasonal loss because this event and its associated H loss enhancement occurred in the declining phase of the known seasonal trend. Determining the conditions under which impulsive H loss dominates seasonal or quiescent loss should be a focus of ongoing and future studies.

water from below, as water is optically thin to dissociation on its topside and H is a minor species. In determining the mechanism of water transport, particular emphasis should be brought to bear on understanding any possible mechanistic differences between water lofting at the time of seasonally strongest circulation, during global dust storms, and during regional dust storms. For modelling work, it should be noted that observed dust-driven circulation-induced temperature enhancements near the winter pole (~ 40 K for our regional storm and ~ 55 K for the Mars Year 34 global storm⁴¹) are typically much larger than those of models (~ 16 K in ref. ²¹ and ~ 20 K in ref. ²²), hinting that models underpredict the circulation strength of the Mars atmosphere during at least some dust events and might therefore also underpredict H loss.

Beyond desiccation, regional dust events are a source of oxidizing power to the planet. All H is lost to space, whereas O can be lost both to space and the Martian crust. Desiccation results from H loss to space no matter the O loss, and oxidation results from more H lost to space than twice the O loss. Our results demonstrate a large enhancement in H loss together with a likely decrease in O loss due to warmer, more collisional thermospheric conditions^{32,42}. Total loss from the atmosphere must be in the 2:1 stoichiometric ratio of water in a steady state with no species other than H and O escaping and with water the only condensable species containing both H and O. With elevated H loss during the storm, more O is left in the atmosphere, which oxidizes the system at least temporarily. Either escape under other conditions is slightly reducing, making up the 2:1 balance over a longer time period, or the O ends up oxidizing the crust. Current estimates of total loss put the H:O escape ratio close to 2:1 on average⁴³; based on our estimated tenfold increase in H loss during the event, and assuming no change in O loss (which is driven by the dissociative recombination of the dominant O_2^+ ion and is unresponsive to H photochemistry^{44,45}), the ratio of escape in dust events is likely to be 10:1 or larger. This excess indicates that

H loss and O loss should not be taken as balanced on seasonal or interannual timescales (as has been assumed in some studies⁴⁶), but only on the closure timescale of all relevant forcing (the steady-state timescale of ref. ⁴⁷), which may not exist.

The time variation of H loss in the geologically recent past is unknown and likely to be strongly affected by the obliquity of Mars, which is variable on timescales longer than 10,000 years⁴⁸. At high obliquity, increased interhemispheric circulation could loft more water to high altitude, potentially increasing H loss. At low obliquity, the opposite could occur, because water and CO_2 would freeze out at the poles⁴⁹ and general circulation would be weaker. Because the long-term average obliquity of the planet is higher than the present value, it is likely that H loss measured today is a lower limit on the time-averaged loss rate. Long-term variations in the argument of perihelion would also contribute to a change in the seasonal cycle, although it is likely that the topographic asymmetry of the northern and southern hemispheres would result in high-altitude water and enhanced H loss in southern summer rather than at perihelion⁵⁰.

On early Mars, the atmosphere was thick enough to support abundant surface liquid water, and may have been thick enough to limit H loss. In dense atmospheres, the temperature profile is set by greenhouse gas radiative-convective balance, as opposed to the dust-controlled temperature profile of the present-day Mars atmosphere. An early thick atmosphere would likely have had a much more effective cold trap, as is the case today at Earth, strictly limiting the ability of dust to raise atmospheric temperatures and enhance H loss. In addition, the wetter surface would have been less conducive to fine dust formation. This suggests that H loss may have reached a tipping point: as the atmosphere thinned due to other escape processes, it crossed a threshold at which dust events could drive loss. Major advances in our understanding will be required to determine whether all Mars-sized planets follow a similar trajectory.

Methods

Observation geometry. The MRO and TGO missions are in relatively stable orbits designed for consistent remote sensing, whereas MAVEN's orbit precesses with time to facilitate broad sampling of the atmosphere with its suite of in-situ instruments. This limits the availability of coronal observations useful for constraining H loss with IUVS.

Coronal observations are made on the outbound and inbound segments of MAVEN's elliptical orbit, when H Lyman α can be observed at high altitude. These observations can be used to constrain H loss when MAVEN's apoapsis is on the dayside at relatively low latitude. As shown in Extended Data Fig. 1, this configuration has occurred only rarely over the course of the MAVEN mission, most notably during the Mars Year 34 C storm that we report on here. Earlier occurrences of this observation geometry did not have corresponding TGO data.

Zooming in on the time period presented here, Extended Data Fig. 2 shows the geometry of the TGO and MAVEN observations during the study period of the Mars Year 34 C storm. The regularity of the MRO/MCS observations obviates the need for visualization, as these observations occur at 15:00 across all latitudes and have been zonally averaged across all longitudes.

MCS data processing. The MCS has nine spectral channels from 0.3 μm to 45 μm (ref. 23). The MCS measures limb (or horizon) radiances from the surface to ~ 90 km with ~ 5 km vertical resolution provided by arrays of 21 detectors for each channel and acquires on-planet observations. The MCS is on the MRO and observes the atmosphere at $\sim 15:00$ (daytime) and $\sim 3:00$ (nighttime) globally on a daily basis⁵¹. Geophysical profiles of temperature, dust opacity (at 22 μm) and water ice (at 12 μm) as well as surface brightness temperature are retrieved from the radiances using a two-dimensional radiative transfer code^{24,25,52}. (The MCS opacities can be converted to visible opacities with a multiplying factor of 7.3 for dust and 3.3 for water ice²².) The specific retrievals used in this work are optimized for the retrieval of dust opacity profiles under major dust storm conditions⁴¹. The aerosol opacity profiles are integrated (after being extended well mixed to the surface for dust) to obtain the column opacities used in this work.

The individual retrieved profiles are then used to calculate a zonal mean value through binning (with bin size of 5° in latitude by 2° in L_s) to match the MCS coverage patterns⁵⁰. This was performed for the temperatures on the 5 Pa pressure surface (~ 50 km above the surface) as well as for the dust and ice column values. The dust column opacity values were filtered to remove CO_2 ice.

NOMAD data processing. The vertical profiles of water vapour volume mixing retrieved by the NOMAD Solar Occultation data shown in this study were presented in ref. 13. Here, a brief summary of the retrieval method is provided. The NOMAD spectra in the diffraction orders 134 ($3,011\text{--}3,035\text{ cm}^{-1}$) and 168 ($3,775\text{--}3,805\text{ cm}^{-1}$), which include strong H_2O lines, were processed. The retrievals were performed with the ASIMUT-ALVL radiative transfer and inversion code⁵³. Absorptions by H_2O and CO_2 molecules were taken into account in the radiative transfer calculation, and the absorption coefficients were calculated using spectroscopic databases: the HITRAN 2016 database⁵⁴ for CO_2 and the water line list for CO_2 -rich atmospheres⁵⁵ for H_2O . The temperature, pressure and CO_2 volume mixing ratio of the simulated atmosphere were obtained from the Global Environmental Multiscale Mars model (GEM-Mars)⁵⁶ which takes into account the effects of the dust storms in Mars Year 34 (ref. 23). The retrievals were performed using the Optimal Estimation Method⁵⁷ for each spectrum at each tangential altitude independently. Finally, the retrieved abundances from each diffraction order were averaged with an interval of 1 km to obtain the vertical profiles.

ACS data processing. The procedure to obtain the water mixing ratio profiles from the occultation data is described in ref. 12. The CO_2 and H_2O abundances from the 1.57 and 1.38 μm spectral regions, respectively, are measured in parallel with a slight altitude shift due to sequential measurements of the diffraction orders, which is accounted for using interpolation. A forward model of transmission is computed using a look-up table of absorption cross-sections (as a function of pressure and temperature) for a corresponding number of atmospheric layers (40 to 130, depending on orbit), and using the spectral line parameters from the HITRAN 2016 database⁵⁴ with a correction coefficient of 1.7 for the H_2O broadening in CO_2 -dominated atmosphere and self-broadening in the case of CO_2 .

To get temperature and pressure, the model fitting is performed on the data of the diffraction order 49 ($6,318\text{--}6,387\text{ cm}^{-1}$), which covers a CO_2 absorption band, including multiple temperature-sensitive lines with different ground state energy (E''). We use a Levenberg–Marquardt iterative scheme⁵⁷ and Tikhonov regularization to smooth the profile and minimize the uncertainties^{58,59}. The hydrostatic equilibrium was taken into account to constrain simultaneous retrieval of temperature and pressure¹². The initial temperature, pressure and CO_2 volume mixing ratio profiles were taken from the Martian Climate Database MCD 5.3 profiles⁶⁰. The retrieval algorithm converges within 4–6 iterations independently of initial assumptions. The H_2O number density and volume mixing ratio are retrieved applying a similar retrieval procedure to the spectra in the diffraction order 56 ($7,217\text{--}7,302\text{ cm}^{-1}$), which encompasses the 1.38 μm water vapour band. Only one free parameter vector is retrieved (the H_2O volume mixing ratio) with the pressure and temperature profile from order 49. The uncertainty on the retrieved

quantities is given by the covariance matrix of the solution. We also account for the Jacobian errors due to the retrieved temperature and pressure. For water vapour, the retrieval accuracy sharply depends on the aerosol loading and, for a clear atmosphere (with an optical depth 0.2), remains better than 1 ppmv at 10–50 km.

IUVS data processing. Data reduction procedures for H Lyman- α data are identical to those described in ref. 36. We present outlimb and outcorona data available on the Planetary Data System Planetary Atmospheres Node, Version 13, Revision 01. For the outlimb data presented, we use only the last outlimb scan, which underlies the outcorona scan. The Lyman- α brightness observed by MAVEN is a function of the H abundance and the solar brightness, for which we correct by using the MAVEN-measured brightness of the Sun⁶¹. Because Mars H Lyman α is optically thick, some of the variation we observe is also due to the viewing geometry. These observations occurred as MAVEN's orbit apoapsis was slowly evolving in the vicinity of the subsolar point, minimizing geometrical effects.

Comparison of water retrievals from TGO and MCS. A comparison of water retrievals during the event is shown in Extended Data Fig. 3. In the Article, we present southern hemisphere retrievals from both TGO instruments, selecting ACS before $L_s 330^\circ$ and NOMAD thereafter. Both instruments show the same overall variations, with ACS retrieving more water near the surface and at altitude during the dust event than NOMAD. NOMAD retrievals extend closer to the gap in observations than ACS retrievals, permitting detection of high-altitude water in the declining phase of the storm near $L_s 335^\circ$. Water estimates retrieved from MCS data by using assumed saturation conditions are mostly higher than the more direct measurements of ACS and NOMAD, suggesting either that water was not saturated in the regions where MCS retrievals were possible or that fast diurnal variation in high-altitude water is required to explain the discrepancy between the datasets. Near the peak of the event, the absence of clouds on which the MCS retrieval depends introduces noise into this retrieval.

Data availability

MCS-derived and IUVS radiance data shown in Fig. 1 are available to the public on the Planetary Data System Planetary Atmospheres Node (MCS, https://atmos.nmsu.edu/data_and_services/atmospheres_data/MARS/mcs.html; IUVS, https://atmos.nmsu.edu/data_and_services/atmospheres_data/MAVEN/maven_iuvs.html). NOMAD and ACS data are available on the Planetary Science Archive of the European Space Agency at <https://archives.esac.esa.int/psa>. Complete datasets of retrieved water abundances from NOMAD are available on the BIRA-IASB data repository at <http://repository.aeronomie.be/?doi=10.18758/71021054>. ACS water data are available at http://exomars.cosmos.ru/ACS_Results_stormy_water_vREzUd4pxG.

Code availability

Figure 1 results from plotting the accessible datasets described previously. The data reduction procedures to produce these data for the MCS, IUVS, NOMAD and ACS datasets are described in the Methods and references therein.

Received: 12 August 2020; Accepted: 7 June 2021;

Published online: 16 August 2021

References

- Owen, T., Maillard, J. P., de Bergh, C. & Lutz, B. L. Deuterium on Mars: the abundance of HDO and the value of D/H. *Science* **240**, 1767–1770 (1988).
- Anderson, D. E. Jr. & Hord, C. W. Mariner 6 and 7 ultraviolet spectrometer experiment: analysis of hydrogen Lyman-alpha data. *J. Geophys. Res. Space Phys.* **76**, 6666–6673 (1971).
- McElroy, M. B. & Donahue, T. M. Stability of the Martian atmosphere. *Science* **177**, 986–988 (1972).
- Parkinson, T. D. & Hunten, D. M. Spectroscopy and aeronomy of O_2 on Mars. *J. Atmos. Sci.* **29**, 1380–1390 (1972).
- Chaffin, M. S. et al. Unexpected variability of Martian hydrogen escape. *Geophys. Res. Lett.* **41**, 314–320 (2014).
- Clarke, J. T. et al. A rapid decrease of the hydrogen corona of Mars. *Geophys. Res. Lett.* **41**, 8013–8020 (2014).
- Bhattacharyya, D., Clarke, J. T., Bertaux, J.-L., Chaufray, J.-Y. & Mayyasi, M. A strong seasonal dependence in the Martian hydrogen exosphere. *Geophys. Res. Lett.* **42**, 8678–8685 (2015).
- Halekas, J. S. Seasonal variability of the hydrogen exosphere of Mars. *J. Geophys. Res. Planets* **122**, 901–911 (2017).
- Heavens, N. G. et al. Hydrogen escape from Mars enhanced by deep convection in dust storms. *Nat. Astron.* **2**, 126–132 (2018).
- Clarke, J. T. Dust-enhanced water escape. *Nat. Astron.* **2**, 114–115 (2018).
- Fedorova, A. et al. Water vapor in the middle atmosphere of Mars during the 2007 global dust storm. *Icarus* **300**, 440–457 (2018).
- Fedorova, A. A. et al. Stormy water on Mars: the distribution and saturation of atmospheric water during the dusty season. *Science* **367**, 297–300 (2020).

13. Aoki, S. et al. Water vapor vertical profiles on Mars in dust storms observed by TGO/NOMAD. *J. Geophys. Res. Planets* **124**, 3482–3497 (2019).
14. Wu, Z., Li, T., Zhang, X., Li, J. & Cui, J. Dust tides and rapid meridional motions in the Martian atmosphere during major dust storms. *Nat. Commun.* **11**, 614 (2020).
15. Liuzzi, G. et al. Strong variability of Martian water ice clouds during dust storms revealed from ExoMars Trace Gas Orbiter/NOMAD. *J. Geophys. Res. Planets* **125**, e2019JE006250 (2020).
16. Connour, K. et al. Mars's twilight cloud band: a new cloud feature seen during the Mars year 34 global dust storm. *Geophys. Res. Lett.* **47**, e2019GL084997 (2020).
17. Stone, S. W. et al. Hydrogen escape from Mars is driven by seasonal and dust storm transport of water. *Science* **370**, 824–831 (2020).
18. Chaffin, M. S., Deighan, J., Schneider, N. M. & Stewart, A. I. F. Elevated atmospheric escape of atomic hydrogen from Mars induced by high-altitude water. *Nat. Geosci.* **10**, 174–178 (2017).
19. Maltagliati, L. et al. Evidence of water vapor in excess of saturation in the atmosphere of Mars. *Science* **333**, 1868–1871 (2011).
20. Maltagliati, L. et al. Annual survey of water vapor vertical distribution and water–aerosol coupling in the Martian atmosphere observed by SPICAM/MEEx solar occultations. *Icarus* **223**, 942–962 (2013).
21. Shaposhnikov, D. S., Medvedev, A. S., Rodin, A. V. & Hartogh, P. Seasonal water ‘pump’ in the atmosphere of Mars: vertical transport to the thermosphere. *Geophys. Res. Lett.* **46**, 4161–4169 (2019).
22. Neary, L. et al. Explanation for the increase in high-altitude water on Mars observed by NOMAD during the 2018 global dust storm. *Geophys. Res. Lett.* **47**, e2019GL084354 (2020).
23. McCleese, D. J. et al. Mars Climate Sounder: an investigation of thermal and water vapor structure, dust and condensate distributions in the atmosphere, and energy balance of the polar regions. *J. Geophys. Res. Planets* **112**, E05S06 (2007).
24. Kleinböhl, A. et al. Mars Climate Sounder limb profile retrieval of atmospheric temperature, pressure, and dust and water ice opacity. *J. Geophys. Res. Planets* **114**, E10006 (2009).
25. Kleinböhl, A., Friedson, A. J. & Schofield, J. T. Two-dimensional radiative transfer for the retrieval of limb emission measurements in the Martian atmosphere. *J. Quant. Spectrosc. Radiat. Transf.* **187**, 511–522 (2017).
26. Korabiev, O. et al. The Atmospheric Chemistry Suite (ACS) of three spectrometers for the ExoMars 2016 Trace Gas Orbiter. *Space Sci. Rev.* **214**, 7 (2018).
27. Vandaele, A. et al. Science objectives and performances of NOMAD, a spectrometer suite for the ExoMars TGO mission. *Planet. Space Sci.* **119**, 233–249 (2015).
28. McClintock, W. E. et al. The Imaging Ultraviolet Spectrograph (IUUVS) for the MAVEN Mission. *Space Sci. Rev.* **195**, 75–124 (2015).
29. Chaffin, M. S. et al. Three-dimensional structure in the Mars H corona revealed by IUUVS on MAVEN. *Geophys. Res. Lett.* **42**, 9001–9008 (2015).
30. Kass, D. M., Kleinböhl, A., McCleese, D. J., Schofield, J. T. & Smith, M. D. Interannual similarity in the Martian atmosphere during the dust storm season. *Geophys. Res. Lett.* **43**, 6111–6118 (2016).
31. Kass, D. et al. Mars Climate Sounder observation of Mars' 2018 global dust storm. *Geophys. Res. Lett.* **47**, e83931 (2020).
32. Jain, S. K. et al. Martian thermospheric warming associated with the Planet Encircling Dust Event of 2018. *Geophys. Res. Lett.* **47**, e85302 (2020).
33. Kockarts, G. & Nicolet, M. Le problème aéronomique de l'hélium et de l'hydrogène neutres. *Ann. Geophys.* **18**, 269 (1962).
34. Mayyasi, M. et al. Significant space weather impact on the escape of hydrogen from Mars. *Geophys. Res. Lett.* **45**, 8844–8852 (2018).
35. Bhattacharyya, D., Clarke, J., Bertaux, J.-L., Chaufray, J.-Y. & Mayyasi, M. Analysis and modeling of remote observations of the Martian hydrogen exosphere. *Icarus* **281**, 264–280 (2017).
36. Chaffin, M. S. et al. Mars H escape rates derived from MAVEN/IUVS Lyman alpha brightness measurements and their dependence on model assumptions. *J. Geophys. Res. Planets* **123**, 2192–2210 (2018).
37. Halekas, J. S. et al. Structure, dynamics, and seasonal variability of the Mars-solar wind interaction: MAVEN Solar Wind Ion Analyzer in-flight performance and science results. *J. Geophys. Res. Space Phys.* **122**, 547–578 (2017).
38. Hughes, A. et al. Proton aurora on Mars: a dayside phenomenon pervasive in southern summer. *J. Geophys. Res. Space Phys.* **124**, 10533–10548 (2019).
39. Montabone, L. et al. Martian year 34 column dust climatology from Mars Climate Sounder observations: reconstructed maps and model simulations. *J. Geophys. Res. Planets* **125**, e2019JE006111 (2020).
40. Heavens, N. G., Kass, D. M. & Shirley, J. H. Dusty deep convection in the Mars Year 34 Planet-Encircling Dust Event. *J. Geophys. Res. Planets* **124**, 2863–2892 (2019).
41. Kleinböhl, A. et al. Diurnal variations of dust during the 2018 global dust storm observed by the Mars Climate Sounder. *J. Geophys. Res. Planets* **125**, e06115 (2020).
42. Elrod, M., Bougher, S., Roeten, K., Murphy, J. & Sharrar, R. Structural and compositional changes in the upper atmosphere related to the PEDE-2018a dust event on Mars as observed by MAVEN NGIMS. *Geophys. Res. Lett.* **47**, e2019GL084378 (2020).
43. Jakosky, B. M. et al. Loss of the Martian atmosphere to space: present-day loss rates determined from MAVEN observations and integrated loss through time. *Icarus* **315**, 146–157 (2018).
44. Deighan, J. et al. MAVEN IUVS observation of the hot oxygen corona at Mars. *Geophys. Res. Lett.* **42**, 9009–9014 (2015).
45. Lillis, R. et al. Photochemical escape of oxygen from Mars: first results from MAVEN in situ data. *J. Geophys. Res. Space Phys.* **122**, 3815–3836 (2017).
46. Krasnopolsky, V. A. Photochemistry of water in the Martian thermosphere and its effect on hydrogen escape. *Icarus* **321**, 62–70 (2019).
47. Fox, J. L. & Hač, A. B. Photochemical escape of oxygen from Mars: a comparison of the exobase approximation to a Monte Carlo method. *Icarus* **204**, 527–544 (2009).
48. Laskar, J. et al. Long term evolution and chaotic diffusion of the insolation quantities of Mars. *Icarus* **170**, 343–364 (2004).
49. Lindner, B. L. & Jakosky, B. M. Martian atmospheric photochemistry and composition during periods of low obliquity. *J. Geophys. Res. Space Phys.* **90**, 3435–3440 (1985).
50. Richardson, M. I. & Wilson, R. J. A topographically forced asymmetry in the Martian circulation and climate. *Nature* **416**, 298–301 (2002).
51. Zurek, R. W. & Smrekar, S. E. An overview of the Mars Reconnaissance Orbiter (MRO) science mission. *J. Geophys. Res. Planets* **112**, E05S01 (2007).
52. Kleinböhl, A., Schofield, J. T., Abdou, W. A., Irwin, P. G. J. & de Kok, R. J. A single-scaling approximation for infrared radiative transfer in limb geometry in the Martian atmosphere. *J. Quant. Spectrosc. Radiat. Transf.* **112**, 1568–1580 (2011).
53. Vandaele, A. C., Kruglanski, M. and de Mazière, M. Modeling and Retrieval of Atmospheric Spectra Using ASIMUT. In *Proc. 1st Atmospheric Science Conference* (ed. Lacoste, H) Vol. 628 (ESA, 2006).
54. Gordon, I. E. et al. The HITRAN2016 molecular spectroscopic database. *J. Quant. Spectrosc. Radiat. Transf.* **203**, 3–69 (2017).
55. Gamache, R. R., Faresse, M. & Renaud, C. L. A spectral line list for water isotopologues in the 1100–4100 cm⁻¹ region for application to CO₂-rich planetary atmospheres. *J. Mol. Spectrosc.* **326**, 144–150 (2016).
56. Neary, L. & Daerden, F. The GEM-Mars general circulation model for Mars: description and evaluation. *Icarus* **300**, 458–476 (2018).
57. Rodgers, C. D. *Inverse Methods for Atmospheric Sounding: Theory and Practice* (World Scientific, 2000).
58. Ceccherini, S. Analytical determination of the regularization parameter in the retrieval of atmospheric vertical profiles. *Opt. Lett.* **30**, 2554–2556 (2005).
59. Ceccherini, S., Belotti, C., Carli, B., Raspollini, P. & Ridolfi, M. Technical Note: Regularization performances with the error consistency method in the case of retrieved atmospheric profiles. *Atmos. Chem. Phys.* **7**, 1435–1440 (2007).
60. Millour, E. et al. The Mars Climate Database (MCD version 5.2). In *Proc. European Planetary Science Congress 2015 EPSC2015-438* (EPSC, 2015).
61. Eparvier, F. G., Chamberlin, P. C., Woods, T. N. & Thiemann, E. M. B. The Solar Extreme Ultraviolet monitor for MAVEN. *Space Sci. Rev.* **195**, 293–301 (2015).

Acknowledgements

This research was supported by NASA through the MAVEN and MRO projects. IUVS data products were produced using the RMACC Summit supercomputer, which is supported by the National Science Foundation (award nos. ACI-1532235 and ACI-1532236), by the University of Colorado Boulder and by Colorado State University. The Summit supercomputer is a joint effort of the University of Colorado Boulder and Colorado State University. M.M.J.C. is supported by the NASA Postdoctoral Program at the NASA Goddard Space Flight Center, which is administered by the Universities Space Research Association under contract with NASA. A.K. acknowledges support from the NASA Mars Data Analysis Program (80NM0018F0719). Work at the Jet Propulsion Laboratory, California Institute of Technology, is performed under contract with NASA. ExoMars is a space mission of the European Space Agency and Roscosmos. The NOMAD experiment is led by the Royal Belgian Institute for Space Aeronomy (BIRA-IASB), assisted by co-principal investigator teams from Spain (IAA-CSIC), Italy (INAF-IAPS) and the United Kingdom (Open University). For this project we acknowledge funding by the Belgian Science Policy Office, with financial and contractual coordination by the European Space Agency Prodex Office (PEA 4000103401 and 4000121493); by the Spanish MICINN through its Plan Nacional; by European funds under grant nos. PGC2018-101836-B-I00 and ESP2017-87143-R (MINECO/FEDER); by the United Kingdom Space Agency through grant nos. ST/R005761/1, ST/P001262/1, ST/R001405/1 and ST/S00145X/1; and by the Italian Space Agency through grant no. 2018-2-HH.0. The IAA-CSIC team acknowledges financial support from the State Agency for Research of the Spanish MCIU through the ‘Center of Excellence Severo Ochoa’ award for the Instituto de Astrofísica de Andalucía (SEV-2017-0709). This work was supported by the Belgian Fonds de la Recherche Scientifique-FNRS under grant nos. 30442502 (ET_HOME) and T.0171.16 (CRAMIC) and by the Belgian Science Policy Office BrainBe

SCOOP Project. S.A. is 'Chargé de Recherches' at the F.R.S.-FNRS. NOMAD's United States investigators are supported by NASA. Science operations of ACS on TGO are funded by Roscosmos and the ESA. IKI affiliates acknowledge support from the Ministry of Science and Higher Education of the Russian Federation. F.M. acknowledges funding from the CNES and ANR (PRCI, CE31 AAPG2019-MCUBE project).

Author contributions

M.S.C. oversaw the study and cross-instrument comparison and performed MAVEN IUVS H data analysis. D.M.K., N.G.H. and A.K. performed MCS data analysis. S.A. analysed the NOMAD data. I.R.T. and J.T.E. calibrated the NOMAD data and planned NOMAD observations, assisted by B.R. F.D. helped assess the scientific relevance of NOMAD detections. A.C.V., M.R.P., G.B. and J.-J.L.-M. supervised the scientific observations of NOMAD. A.A.F. performed the TGO/ACS data analysis. J.D. identified the event in the IUVS data and suggested follow-up. K.C. provided IUVS apoapsis images of clouds. All authors made significant contributions to understanding or operating the instruments for which data are presented and participated in the preparation of the manuscript text.

Competing interests

The authors declare no competing interests.

Additional information

Extended data is available for this paper at <https://doi.org/10.1038/s41550-021-01425-w>.

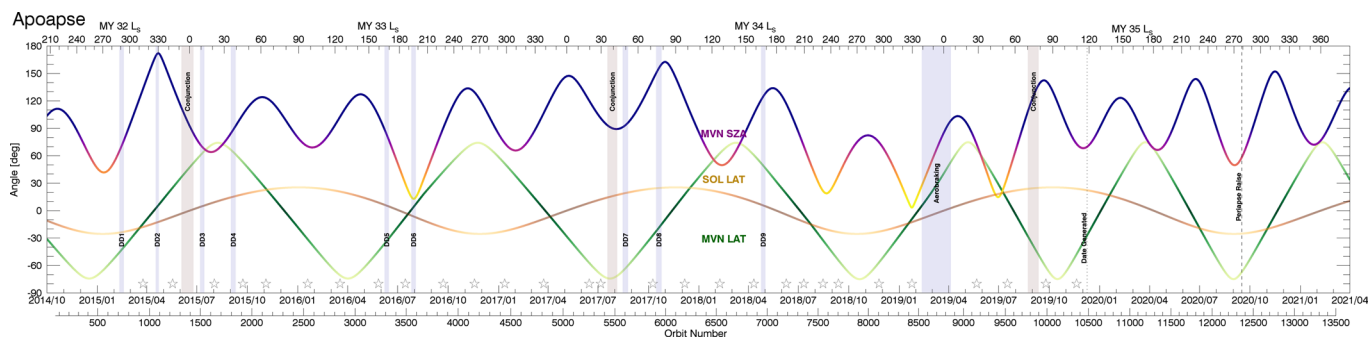
Correspondence and requests for materials should be addressed to M.S.C.

Peer review information *Nature Astronomy* thanks Claire Newman and the other, anonymous, reviewer(s) for their contribution to the peer review of this work.

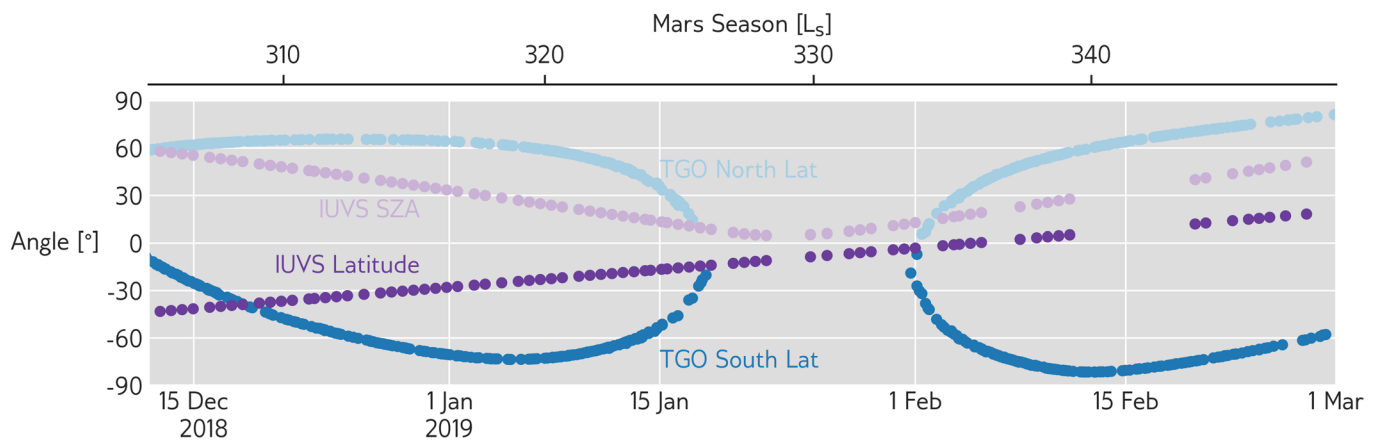
Reprints and permissions information is available at www.nature.com/reprints.

Publisher's note Springer Nature remains neutral with regard to jurisdictional claims in published maps and institutional affiliations.

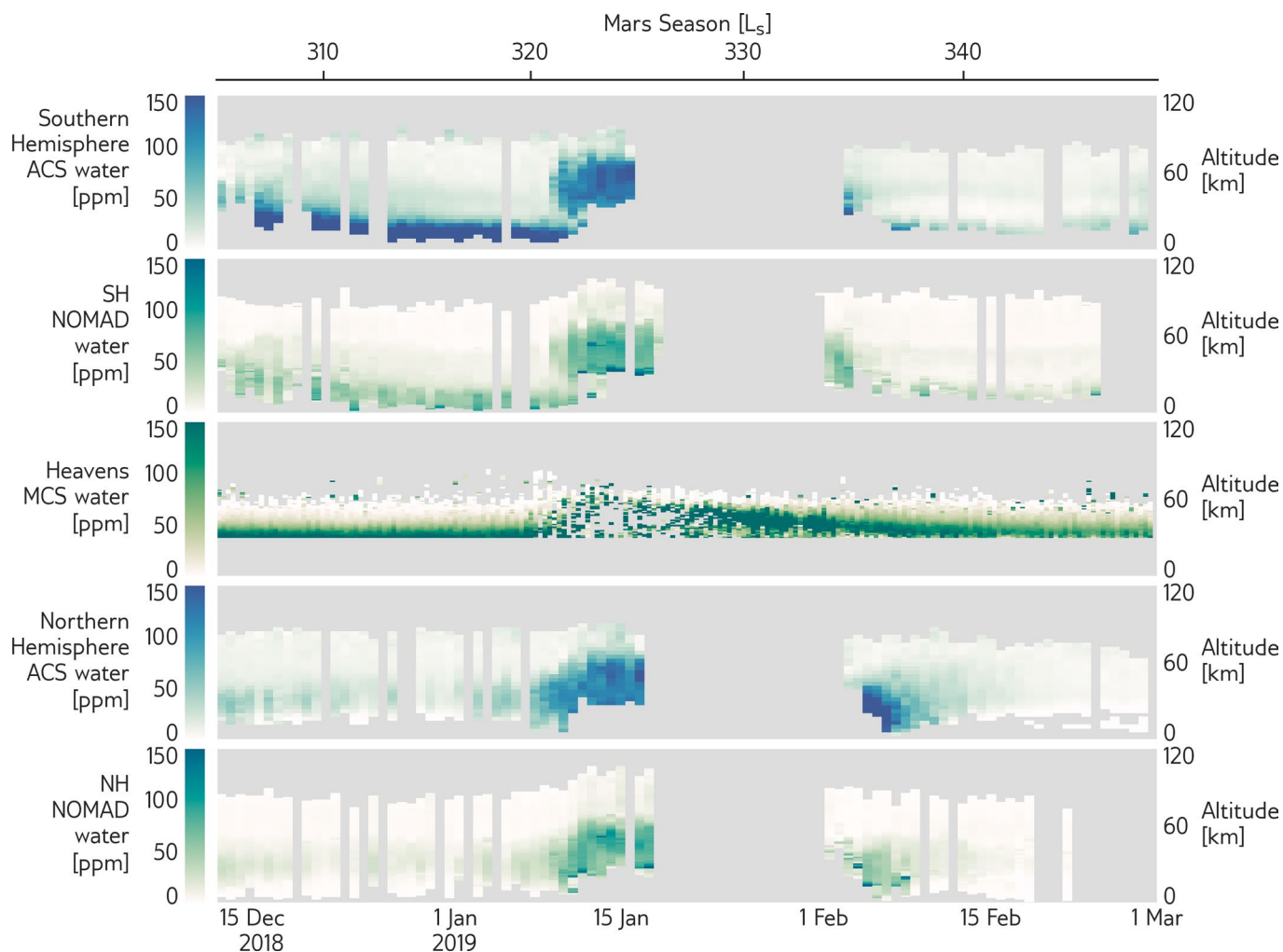
© The Author(s), under exclusive licence to Springer Nature Limited 2021



Extended Data Fig. 1 | Geometry of MAVEN apoapsis location throughout the MAVEN mission. MAVEN orbit numbers and Earth Year/Month dates are shown on the bottom axis, with Mars Year and L_s on the top axis. The blue/brown and green curves show the location of MAVEN's apoapsis in solar zenith angle (SZA) and local time, and in geographic latitude, respectively. The tan curve shows the latitude of the subsolar point. Intermittent spacecraft activities such as MAVEN Deep Dips (DD-X), Earth-Sun-Mars conjunctions, and the recent aerobraking campaigns are also indicated. IUVS Stellar occultation campaigns are indicated with the star icons. Time periods useful for IUVS H loss measurements occur when apoapsis SZA and latitude are both close to zero and occur relatively rarely in the dataset. Unfortunately these time periods are relatively rare in the dataset.



Extended Data Fig. 2 | Geometry of TGO and IUVS observations shown in Fig. 1. Points show the Mars surface geometry of the point along the observation line of sight with minimum ray height. For TGO, occultations are made in both hemispheres, but Fig. 1 shows only Southern Hemisphere data. MCS observations are made at 3 PM across all latitudes, and zonally averaged across longitudes, and so are not shown here. Both TGO and IUVS observing geometry evolved with time over the period of the study, with minimal impact on the conclusion that regional storms can make possible large amounts of high-altitude water that subsequently increases coronal H abundances and loss rates.



Extended Data Fig. 3 | Comparison of middle atmosphere water retrievals. From top to bottom, water retrieved in the Northern Hemisphere by ACS and NOMAD; MCS water retrievals using the methods of Heavens et al. 2018; and Southern Hemisphere water retrievals from ACS and NOMAD. Data presented in the text comes from the Southern Hemisphere, from ACS before Ls 330, and from NOMAD afterward. Color scales are unique to each instrument for clarity, but because these schemes are perceptual the perceived darkness in each panel is a trustworthy indicator of the water abundance retrieved. ACS retrieved abundances are higher than NOMAD abundances and display larger variations; MCS retrievals are higher than both and limited in altitude range.